



GRB 210610B: The Internal and External Plateau as Evidence for the Delayed Outflow of Magnetar

Yi-Ning Wei (韦逸宁)^{1,2}, Xiang-Gao Wang (王祥高)^{1,2} , Da-Bin Lin (林达斌)^{1,2} , Wei-Kang Zheng (郑伟康)³ ,
Liang-Jun Chen (陈良军)^{1,2} , Sheng-Yu Yan (闫圣钰)⁴, Shuang-Xi Yi (仪双喜)⁵ , Qi Wang (王琦)^{1,2}, Zi-Min Zhou
(周子民)^{1,2}, Hui-Ya Liu (刘慧亚)^{1,2}, and En-Wei Liang (梁恩维)^{1,2} 

¹ Guangxi Key Laboratory for Relativistic Astrophysics, School of Physical Science and Technology, Guangxi University, Nanning 530004, China; wangxg@gxu.edu.cn

² GXU-NAOC Center for Astrophysics and Space Sciences, Nanning 530004, China

³ Department of Astronomy, University of California, Berkeley, CA 94720-3411, USA

⁴ Department of Physics and Tsinghua Center for Astrophysics (THCA), Tsinghua University, Beijing 100084, China

⁵ School of Physics and Physical Engineering, Qufu Normal University, Qufu 273165, China

Received 2024 March 8; revised 2024 May 1; accepted 2024 May 7; published 2024 July 8

Abstract

After launching a jet, outflows of magnetar were used to account for the achromatic plateau of afterglow and the early X-ray flux plateau known as “internal plateau”. The lack of detecting magnetic dipole emission together with the energy injection feature in a single observation poses confusion until the long gamma-ray burst (GRB) 210610B is detected. GRB 210610B is presented with an optical bump following an early X-ray plateau during the afterglow phase. The plateau followed by a steep decline flux overlays in the steadily decaying X-ray flux with index $\alpha_{X,1} \sim 2.06$, indicating an internal origin and that can be fitted by the spin-down luminosity law with the initial plateau luminosity $\log_{10} L_X \sim 48.29 \text{ erg s}^{-1}$ and the characteristic spin-down timescale $T \sim 2818 \text{ s}$. A subsequent bump begins at $\sim 4000 \text{ s}$ in the R band with a rising index $\alpha_{R,1} \sim -0.30$ and peaks at $\sim 14125 \text{ s}$, after which a decay index $\alpha_{R,2} \sim 0.87$ and finally transiting to a steep decay with $\alpha_{R,3} \sim 1.77$ achieve the closure relation of the external shock for the normal decay phase as well as the magnetar spin-down energy injection phase, provided that the average value of the photon index $\Gamma_\gamma = 1.80$ derived from the spectral energy distributions (SEDs) between the X-ray and optical afterglow. The closure relation also works for the late X-ray flux. Akin to the traditional picture of GRB, the outflow powers the early X-ray plateau by dissipating energy internally and collides with the leading decelerating blast burst as time goes on, which could interpret the exotic feature of GRB 210610B. We carry out a Markov Chain Monte Carlo simulation and obtain a set of best parameters: $\epsilon_B \simeq 4.7 \times 10^{-5}$, $\epsilon_e \simeq 0.15$, $E_{K,\text{iso}} \simeq 4.6 \times 10^{53} \text{ erg}$, $\Gamma_0 \simeq 832$, $A_* \simeq 0.10$, $L_{\text{inj},0} \simeq 3.55 \times 10^{50} \text{ erg s}^{-1}$. The artificial light curve can fit the afterglow data well. After that, we estimated the average Lorentz factor and the X-ray radiation efficiency of the later ejecta are 35% and 0.13%, respectively.

Key words: (stars:) gamma-ray burst: individual (GRB 210610B) – (stars:) gamma-ray burst: general – stars: jets

1. Introduction

Gamma-ray bursts (GRBs) signaling the most energetic explosions known in the universe, have at least two distinct physical origins (Zhang et al. 2007a; Zhang 2018), either being linked to the death of massive stripped-envelope star or stemming from mergers of binary compact objects (Eichler et al. 1989; Paczynski 1991; Woosley 1993; Paczyński 1998; Gehrels et al. 2005; Woosley & Bloom 2006; Zhang 2006; Zhang et al. 2007b, 2009; Berger 2014; Abbott et al. 2017; Yang et al. 2022). The central engine driving GRBs could be a new-born black hole (BH) with hyper-accretion, or a rapidly spinning, highly magnetized neutron star (NS; also known as millisecond magnetar). Both of these powerful entities are capable of launching a relativistic jet, in which interactions within the outflow itself produce sub-MeV emission while

subsequent interactions between the outflow with circumburst medium arise afterglow.

Although afterglows are the natural expectation from GRBs and have been widely researched in theory before being detected by BeppoSAX (Costa et al. 1997; Frail et al. 1997; van Paradijs et al. 1997), the successful launches of a series of satellites for X-ray astronomy (in particular the Swift Gamma-Ray Burst Explorer) enable some systematic works to shed more light on afterglows studies (Nousek et al. 2006; Zhang 2006). The lightcurves of the afterglow in X-ray band can usually be divided into four segments: I: the early-time steep decay phase, which is generally interpreted as the so-called curvature effect due to the delay of propagation of photons from high latitudes with respect to the line of sight (Fenimore et al. 1996; Kumar & Panaitescu 2000;

Dermer 2004; Qin et al. 2004; Liang et al. 2006; Zhang et al. 2006); II: the shallow decay phase due to continuous energy injection to the blast wave (Nousek et al. 2006; Zhang et al. 2006; Liang et al. 2007), which is also the definition of “external plateau”; III: the normal decay phase consists with the expectation of the external shock; IV: the late time steeper than normal decay phase due to jet break (Liang et al. 2008; Racusin et al. 2009). Some unusual traits during the afterglow phase were manifested as extended engine activity, such as erratic X-ray flares and early time X-ray plateau superimposed on a background power-law decay afterglow component (known as “internal plateau”). Generally, the energy injection model has been widely adopted to interpret the “external plateau”, which exists in the late time afterglow and has various forms. One of the most popular energy inject forms is that a new-born magnetar loses its rotation energy through dipole radiation and injects into the external shock as $dE_{\text{inj}}/dt \propto (1 + t/\tau)^{-2}$ (Dai & Lu 1998; Yu et al. 2015). In this case, one should detect an attendant involved in the internal dissipation of wind, which however, has never been detected in previous bursts. The puzzle not only makes the explanation of external shock plateau strain but also intrigues us in searching for this signal.

Fortunately for GRB 210610B, which is characterized by a long-lasting optical plateau, is an ideal example that meets the expectations. In early phase, there is an X-ray plateau superposed to the stable decay; onward the abrupt decline appeared at the end of the plateau. Such picture is inconsistent with the so-called standard forward shock afterglow model, but instead is called for the prolonged activity of the central engines.

This paper is organized as follows: The observational information of GRB 210610B is presented in Section 2. In Section 3, we present the results of temporal and spectral analyses. The modeling methods and results are described in Section 4. We conclude our work and make a discussion in Section 5. The temporal and spectral slopes are defined as $F \propto t^{-\alpha} \nu^{-\beta}$ throughout this paper. A concordance cosmology with parameters $H_0 = 70 \text{ km s}^{-1} \text{ Mpc}^{-1}$, $\Omega_M = 0.30$ and $\Omega_\Lambda = 0.70$ is adopted to calculate the luminosity of X-ray plateau.

2. Observations

GRB 210610B was triggered by the Burst Alert Telescope (BAT) onboard Swift on June 10, 2021, at 19:51:27 UT with $T_{90} \simeq 69 \text{ s}$ (Krimm et al. 2021; Page et al. 2021). At 22 s prior to the Swift detection, the Gamma-Ray Burst Monitor (GBM) onboard Fermi had already triggered GRB 210610B (trigger 645047470/210610827) at 19:51:05 UT (T_0) with $T_{90} \simeq 55 \text{ s}$ (Malacaria et al. 2021). The High Energy X-ray telescope (HE) onboard the Hard X-ray Modulation Telescope (HXMT), also trigger at 2021 June 10 19:49:47.510 UT, much earlier than others GRB detector. The lightcurves exhibited a complex

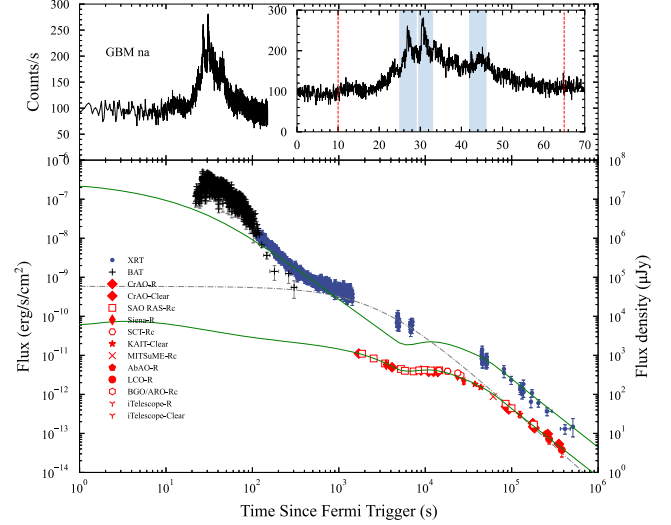


Figure 1. Upper panel: The GBM light curve in gamma-ray band. The time period intercepted by the vertical red dotted line is used for the time-integrated spectrum analysis. The shaded areas are used for the time-resolved spectral analysis. Lower panel: The R -band and X-ray light curve of GRB 210610B afterglow fitted with the external forward shock model. The green solid lines denote the external forward shock model with the wind medium case. The R band frequency is below the characteristic frequency ν_m , flattening before $\sim 2000 \text{ s}$ which we discuss in detail in Section 5. The black “+” symbol is prompt X-ray data in the XRT band (0.3–10 keV) extrapolated from Swift/BAT, and blue dots are the XRT data. The zero-time has been unified as GBM trigger time.

multipulse profile. The X-ray Telescope (XRT) and UV-optical Telescope (UVOT) onboard Swift promptly began observing the field at 83.9 s and 91 s respectively, after the BAT trigger (Page et al. 2021).

We downloaded the BAT and XRT data from the Swift burst analyzer website (Evans et al. 2010)⁶, as well as downloaded the Fermi/GBM data from the Fermi FTP Archive website.⁷ HXMT data were also downloaded from HXMT archive data website.⁸ Their lightcurves were shown in Figure 1. Both the time-integrated and time-resolved spectra of GBM were extracted by a Python source package gtBurst.⁹ About 3.14 days after trigger, we used Las Cumbres Observatory Global Telescope (LCOGT) 1.0 m Sinistro instruments to conduct optical follow-up observations of GRB 210610B. A set of $5 \times 300 \text{ s}$ exposures were performed in Bessel R filters. Data reduction was carried out following standard routines in IRAF¹⁰ package. The photometric data is shown in Table 1. The optical afterglow data are also shown in Figure 1.

⁶ http://www.swift.ac.uk/burst_analyser/01054681/

⁷ <ftp://legacy.gsfc.nasa.gov/fermi/data/>

⁸ <http://archive.hxmt.cn/grb>

⁹ <https://github.com/giacomov/gtburst>

¹⁰ IRAF is distributed by the National Optical Astronomy Observatory (NOAO), which is operated by AURA, Inc., under a cooperative agreement with the NSF.

Table 1
Optical Afterglow Photometry Log of GRB 210610B

$T - T_0$ (mid, s) ^a	Exp.(s)	Mag ^b	σ ^c	Filter	Telescope
1704	10	16.11	0.02	<i>R</i>	CrAO, 30178, (1)
4130	10	16.99	0.02	<i>R</i>	CrAO, 30178, (1)
86208	120	19.50	0.12	<i>R</i>	CrAO, 30213, (2)
177531	2 × 120	20.80	0.10	<i>R</i>	CrAO, 30245, (2)
183898	2 × 120	20.89	0.10	<i>R</i>	CrAO, 30245, (2)
351229	25 × 120	21.90	0.11	<i>R</i>	CrAO, 30245, (2)
3535	300	16.83	0.04	<i>R</i>	Siena, 30198, (3)
23695	300	17.52	0.16	<i>R</i>	Siena, 30198, (3)
27955	5 × 300	17.95	0.12	<i>R</i>	iTelescope, 30231, (4)
249341	72 × 60	21.25	0.14	<i>R</i>	AbAO, 30243, (2)
271450	5 × 300	21.60	0.27	<i>R</i>	LCOGT
380500	5 × 300	22.29	0.37	<i>R</i>	LCOGT
85085	4 × 300	19.33	0.01	<i>R</i>	SAO RAS, 30230, (5)
99648	5 × 300	19.62	0.02	<i>R</i>	SAO RAS, 30230, (5)
181028	6 × 300	20.67	0.06	<i>R</i>	SAO RAS, 30230, (5)
1858	20	16.15	0.01	<i>Rc</i>	SAO RAS, 30187, (6)
2531	60	16.43	0.01	<i>Rc</i>	SAO RAS, 30187, (6)
3427	60	16.75	0.01	<i>Rc</i>	SAO RAS, 30187, (6)
5234	60	17.13	0.01	<i>Rc</i>	SAO RAS, 30187, (6)
5825	60	17.22	0.01	<i>Rc</i>	SAO RAS, 30187, (6)
7337	60	17.26	0.01	<i>Rc</i>	SAO RAS, 30187, (6)
8518	60	17.19	0.01	<i>Rc</i>	SAO RAS, 30187, (6)
9898	180	17.17	0.01	<i>Rc</i>	SAO RAS, 30187, (6)
11596	120	17.20	0.01	<i>Rc</i>	SAO RAS, 30187, (6)
14494	120	17.19	0.01	<i>Rc</i>	SAO RAS, 30187, (6)
14365	5 × 180	17.20	0.07	<i>Rc</i>	SCT, 30205, (7)
18045	5 × 180	17.25	0.08	<i>Rc</i>	SCT, 30205, (7)
23782	900	17.36	0.05	<i>Rc</i>	BGO/ARO, 30228, (8)
25942	840	17.50	0.08	<i>Rc</i>	BGO/ARO, 30228, (8)
61200	9780	18.90	0.10	<i>Rc</i>	MITSuME, 30220, (9)
8915	5 × 300	17.20	0.03	<i>Clear</i>	CrAO, 30988, (2)
10959	5 × 300	17.28	0.08	<i>Clear</i>	CrAO, 30988, (2)
12471	5 × 300	17.28	0.06	<i>Clear</i>	CrAO, 30988, (2)
13983	5 × 300	17.29	0.06	<i>Clear</i>	CrAO, 30988, (2)
88293	8 × 300	19.58	0.10	<i>Clear</i>	CrAO, 30988, (2)
89967	6 × 300	19.50	0.09	<i>Clear</i>	CrAO, 30988, (2)
92537	17 × 300	19.69	0.09	<i>Clear</i>	CrAO, 30988, (2)
175828	14 × 300	20.57	0.19	<i>Clear</i>	CrAO, 30988, (2)
261443	20 × 300	21.26	0.17	<i>Clear</i>	CrAO, 30988,(2)
3535	7 × 60	16.79	0.05	<i>Clear</i>	iTelescope, 30231, (4)
27235	2 × 300	17.76	0.02	<i>Clear</i>	iTelescope, 30231, (4)
37678	60 × 60	18.07	0.05	<i>Clear</i>	KAIT, 30204, (10)
43942	60 × 60	18.27	0.06	<i>Clear</i>	KAIT, 30204, (10)
124438	30 × 60	20.00	0.20	<i>Clear</i>	KAIT, 30227, (10)

Notes. References:(1) Rumyantsev et al. (2021); (2) Pankov et al. (2021a, 2021b, 2021c, 2021d); (3) Marchini et al. (2021); (4) Nissinen & Oksanen (2021); (5) Moskvitin et al. (2021); (6) Moskvitin & GRB follow-up Team (2021); (7) Vreeswijk & Broens (2021); (8) Romanov & Lane (2021); (9) Noto et al. (2021); (10) Zheng et al. (2021a, 2021b).

^a $T - T_0$ is the midpoint of each observation, where T_0 is the Fermi/GBM trigger time.

^b The Galactic extinction are not corrected.

^c The uncertainty in the magnitude.

In addition, we also collected the optical data from Gamma-ray Coordination Network (GCN) for our analysis, including observations from SAO RAS 1 m telescope (Moskvitin & GRB follow-up Team 2021; Moskvitin et al. 2021), ZTSh 2.6 m telescope of CrAO observatory (Pankov et al. 2021c, 2021d;

Rumyantsev et al. 2021), 0.3 m telescope at University of Siena Observatory (Marchini et al. 2021), 0.28 m f7 SCT telescope (Vreeswijk & Broens 2021), 0.76 m Katzman Automatic Imaging Telescope (Zheng et al. 2021a, 2021b), MITSuME 50 cm telescope Akeno (Noto et al. 2021), AS-32 telescope of

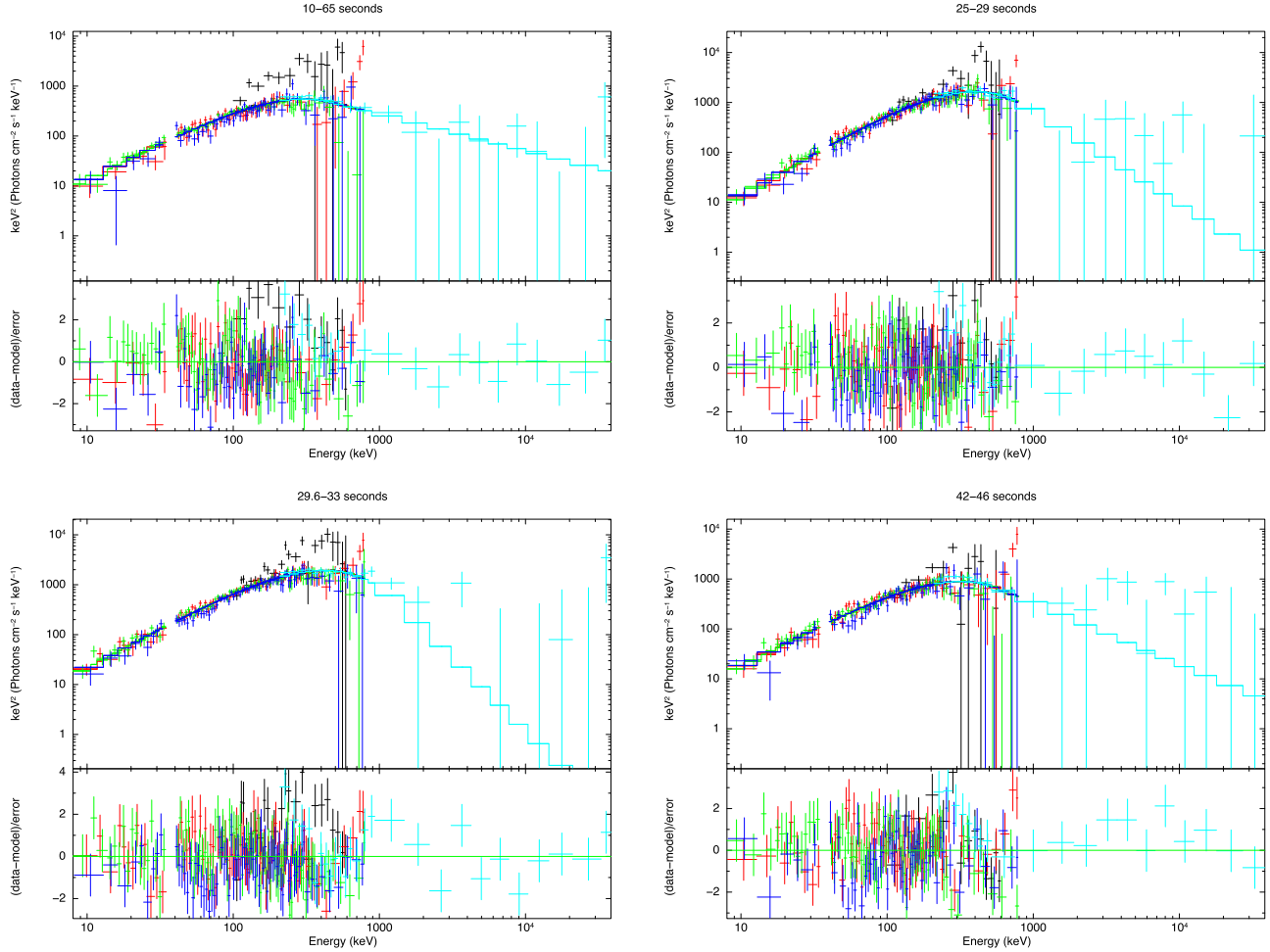


Figure 2. Upper left panel shows the spectral fitting result in the γ -ray pulse period of $t \in [10, 65]$ s. Upper right panel and lower two panels hold similar fitting results in the period from $t \in [25, 29]$ s, $t \in [29.6, 33]$ s, and $t \in [42, 46]$ s, respectively. The HXMT data are marked with the blue cross. The four colors (blue, green, red, blue) correspond to data from Fermi detector (na, nb, n9, b1).

Abastumani observatory (Pankov et al. 2021b), Zeiss 1-m telescope of Simeiz observatory (Ibrahimov et al. 2021), 0.61 m $f/6.5$ telescopes of Burke-Gaffney Observatory (Romanov & Lane 2021), The 0.76 m Katzman Automatic Imaging Telescope (KAIT), and remote telescope T18(0.32 m $f/8.0$ reflector+CCD) of iTelescope (Nissinen & Oksanen 2021; Romanov 2021). Thanks for almost the same central wavelengths, R and R_c together with *Clear* can be treated as the same band and not have to calibrate the data with a presumed optical spectral index.

3. Data Analysis

3.1. Prompt Emission

As shown in Figure 1 upper panel, the prompt emission of GRB 210610B shows three prominent pulses: intense interaction between inhomogeneous outflows makes the first pulse

spike, peaking in subsequent pulse and decaying below the detection threshold after the last smaller amplitude pulse. By combining the GBM data from three sodium iodide (NaI) detectors (na, nb, n9) and one bismuth germanate (BGO) detector (b1), along with HXMT data from CsI phoswich detectors, we were able to construct the time-resolved spectra for each individual pulse as well as time-integrated spectra for overall prompt emission. All spectra were fitted by Band (Band et al. 1993) function and the fitting results are shown in Figure 2, also given in Table 2. The fitting results indicate no significant evolution across three pulses, encompassing low-energy photon index $\hat{\alpha}$, high-energy photon index $\hat{\beta}$, and the peak energy E_p related to the break energy E_c via the relation $(2 + \hat{\alpha})E_c$. Although a more detailed spectral analysis could be conducted given the brightness of the prompt emission, it exceeds the scope of this work.

Table 2

Spectral Fit for the Prompt Emission of GRB 210610B with the Band Function

Time Interval (s)	$\hat{\alpha}$	$\hat{\beta}$	E_p (keV)	χ_r^2
[10, 65]	-0.47 ± 0.05	-2.73 ± 0.22	305 ± 24	0.94
[25, 29]	-0.22 ± 0.04	-3.86 ± 1.18	402 ± 25	1.21
[29.6, 33]	-0.37 ± 0.03	-4.77 ± 3.86	420 ± 23	1.56
[42, 46]	-0.43 ± 0.06	-3.23 ± 0.72	319 ± 30	1.04

We noted the hard low-energy photon index corresponding to spectral index $\hat{\alpha} + 1$, exceeds the so-called ‘‘synchrotron line of death,’’ $F_\nu \propto \nu^{1/3}$, which may be responsible for additional mechanisms at play during the prompt emission, such as photosphere emission (Chen et al. 2022).

The isotropic energy of the prompt emission could be estimated as:

$$E_{\gamma, \text{iso}} = \frac{4\pi D_L^2 k S_\gamma}{1 + z}, \quad (1)$$

where D_L is the luminosity distance, k is a factor to correct the observed γ -ray energy into a broader bandpass (e.g., $1\text{--}10^4$ keV in the rest frame) using the observed GRB spectra (Wang et al. 2015), and S_γ is the γ -ray fluence. For GRB 210610B, with $z = 1.1345$ (de Ugarte Postigo et al. 2021), we calculated D_L to be 2.38×10^{28} cm.

The fluxes are integrated from $T_0 + 10$ s to $T_0 + 65$ s in 8–1000 keV to calculate the γ -ray fluence $S_\gamma = (1.37 \pm 0.19) \times 10^{-4}$ erg cm $^{-2}$, with which we infer the isotropic energy of $E_{\gamma, \text{iso}} = (5.55 \pm 0.78) \times 10^{53}$ erg. The isotropic energy $E_{\gamma, \text{iso}}$ and peak energy E_p of GRB 210610B obey the Amati relation (Amati et al. 2002) given by Wang et al. (2018), shown in Figure 3.

3.2. Afterglow Emission

To investigate the afterglow properties of GRB 210610B, we undertake comprehensive temporal and spectral analysis. A single power-law (SPL) function and a smoothly broken power-law (BPL) function have been commonly used to describe the evolution of the afterglow light curves (Liang et al. 2009; Pozanenko et al. 2013; Wang et al. 2015). The SPL is expressed as:

$$F_1 = F_{01} t^{-\alpha}, \quad (2)$$

where F_{01} is the flux normalization and α is the decay slope. The BPL function is expressed as:

$$F_2 = F_{02} \left[\left(\frac{t}{t_b} \right)^{\omega \alpha_1} + \left(\frac{t}{t_b} \right)^{\omega \alpha_2} \right]^{-1/\omega}, \quad (3)$$

where F_{02} is the flux normalization factor, α_1 , α_2 are decay indices before and after break time t_b , respectively. ω represents the sharpness of the break.

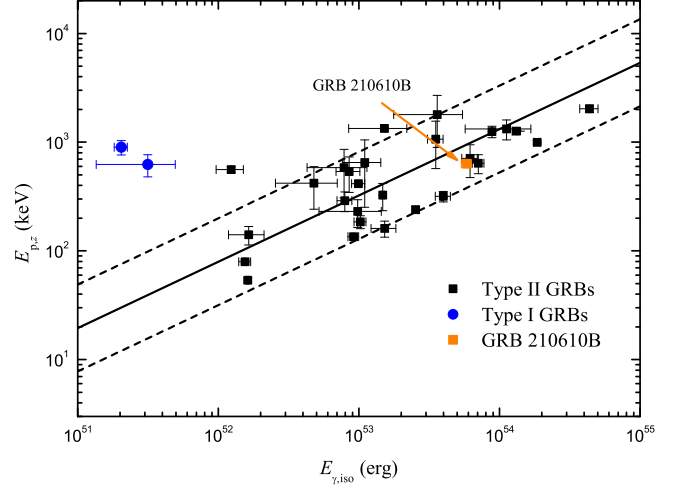


Figure 3. Type I and Type II denote massive mass origin and compact star origin, respectively. The Amati relation $\frac{E_{p,z}}{100\text{keV}} \simeq (0.63 \pm 0.31) \left(\frac{E_{\gamma, \text{iso}}}{10^{52}\text{erg}} \right)^{0.69 \pm 0.07}$ referred to Wang et al. (2018) are shown with the solid line.

Theoretically, there are two cases in the afterglow model due to the energy injection being over abruptly. If the ending time of energy injection comes up before $1/\Gamma$ (the reverse of the bulk Lorentz factor of jet) drops below the jet opening angle θ_j , ‘‘normal decay’’ arises in the gap. Otherwise, since energy injects into the blast wave continuously, the afterglow flux decays shallower than the expectation after jet break. In any case, to be more flexible, a smooth triple power-law (STPL) function can be employed and is expressed as:

$$F_3 = (F_2^{-\omega_2} + F_4^{-\omega_2})^{-1/\omega_2} \quad (4)$$

where ω_2 is the sharpness of the second break ($t_{b,2}$), and

$$F_4 = F_2(t_{b,2}) \left(\frac{t}{t_{b,2}} \right)^{-\alpha_3} \quad (5)$$

As shown in Figure 4, the optical photometric observations commenced ~ 1682 s after the explosion. The R band light curve initially shows a power decay until $t \gtrsim 3 \times 10^3$ s, but after that it behaves as a long-lived bump (plateau) and is followed by a power-law decay tail. Consequently, we adopt an STPL function to fit the R band light curve. The breaks in most X-ray and optical light curves can be well fit with $\omega = 3$, which is consistent with the fit results using other empirical models (e.g., Willingale et al. 2007; Liang et al. 2008; Wang et al. 2015). In our fitting, the sharpness parameter ω (ω_2) is adopted as 3. The fitting results are presented in Figure 4 and Table 3. Our fitting results show that the long-lived bump (plateau) in the R band has $\alpha_{R,1} = -0.30 \pm 0.02$ (again $F \propto t^{-\alpha} \nu^{-\beta}$). After peaking at ~ 14125 s, it transfers to a power-law decay with

Table 3
Temporal Analysis of the Afterglow of GRB 210610B

Band	Model	α_1	α_2	t_b (s)	α_3	$t_{b,2}$
R	STPL	$-0.30^{+0.02}_{-0.02}$	$0.85^{+0.05}_{-0.06}$	14125^{+329}_{-322}	$1.73^{+0.05}_{-0.05}$	63096^{+22018}_{-17387}
XRT	STPL	$2.06^{+0.05}_{-0.05}$	$-0.30(\text{fixed})$	$4000(\text{fixed})$	$1.81^{+0.09}_{-0.09}$	44668^{+32956}_{-18366}

Note. The best fitting parameters are obtained in MCMC with 1σ error.

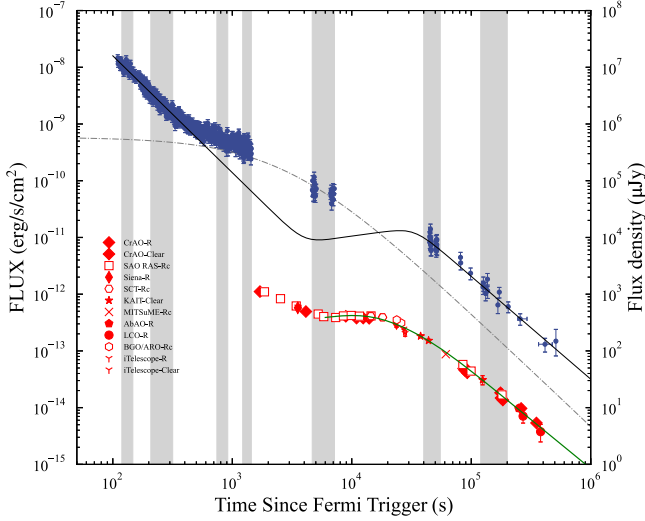


Figure 4. The empirical function fits the XRT and R-band data using STPL functions depicted by black solid line and green solid line, respectively. The gray dotted-dashed line represents an excess on the normal SED decay X-ray afterglow. Several gray-shaded areas are the time slices for SED analysis.

$\alpha_{R,2} = 0.87 \pm 0.06$. Subsequently, it undergoes an even steeper decay, characterized by $\alpha_{R,3} = 1.77 \pm 0.07$.

The X-ray light curve fitting employs the STPL function but masks an excess of about 400 s to 7000 s. At the early phase of the afterglow, the X-ray flux continuously decays with $\alpha_{X,1} = 2.06 \pm 0.05$, followed by a potential bump (plateau) with $\alpha_{X,2} = -0.30$ (fixed) around 5×10^3 s. After the break time $t_2 = 4.5^{3.3}_{1.8} \times 10^4$ s, the light curve decays as a power law with index $\alpha_{X,2} = 1.81 \pm 0.09$. In phase $7 \times 10^3 - 4 \times 10^4$ s, due to the deficiency of data, the break time is rather poorly constrained. We adopted with $\omega_2 = 3$

The X-ray plateau followed by a steep decay at early time generally involves with the spin-down of a magnetar (Troja et al. 2007; Lyons et al. 2010). The luminosity of magnetic dipole torque is $L_{EM} = B^2 R^6 \Omega^4 / 6c^2 = L_0 (1 + t/\tau)^{4/1-n}$, where $L_0 \equiv B^2 R_0^6 \Omega^4 / 6c^2 \simeq 10^{49} B_{15}^2 P_{-3}^{-4} R_6^6 \text{ erg s}^{-1}$ is the initial luminosity corresponding to the initial angular velocity, $\tau \simeq 2.05 \times 10^3 I_{45} B_{15}^{-2} P_{-3}^2 R_6^{-6}$ s is the spin-down timescale and n is the breaking index. Assuming the efficiency of spin-down luminosity emitted in X-ray band is η_X , then we have $L_{X,iso} = \eta_X L_{EM}' =$

$L_X (1 + t/T)^{4/1-n}$, where $T = \tau(1 + z)$. Therefore, the early time X-ray plateau followed by the steep decay of X-ray afterglow light curve can be fitted with $F_X = (1 + z)(L_{X,iso} + At^{-\alpha}) / (4\pi D_L^2)$, where z is redshift, and D_L is the corresponding luminosity distance. We fix α to be 2.05 from the above results and the obtained parameters are: $\log_{10} A = 53.71^{+0.01}_{-0.01}$, $\log_{10} L_X = 48.29^{+0.02}_{-0.02} \text{ erg s}^{-1}$, $T = 2818^{+133}_{-248}$ s, and $n = 3.04^{+0.13}_{-0.10}$.

Before performing the spectral fitting, it is crucial to correct both the X-ray and optical data for Galactic and intrinsic absorption effects. Similarly, correction for the extinction of optical data owing to dust grains in our Galaxy as well as in the host galaxy. The Galactic absorption in the direction of burst with $N_H = 3.94 \times 10^{20} \text{ cm}^{-2}$ is adopted from the UK Swift Science Data Center at the University of Leicester.¹¹ The intrinsic absorption has been fixed to the $N_H^{\text{host}} = 1.25 \times 10^{21} \text{ cm}^{-2}$ estimated from the spectral analysis of late-time (40–1000 ks) XRT data. Galactic extinction correction has been made based on the burst direction (Schlafly & Finkbeiner 2011). The host galaxy extinction is assumed to be characterized by the extinction curves of the Small Magellanic Cloud (SMC) with $R_V = 2.93$ (Pei 1992). We utilize the Xspec package to fit X-ray spectra and extrapolate the unabsorbed power-law spectrum to the optical band. Seven epochs of time-resolved spectra were extracted for fitting, with some photon index rather poorly constrained owing to the sparse data. The results of spectral fitting are shown in Table 4 and Figure 5. We adopt $\Gamma_\gamma = 1.80$ as an average value, which aligns with the value derived from X-ray spectral fitting at the late-time epoch (40–1000 ks).

The spectral index $\beta = \Gamma_\gamma - 1 = 0.80$ can be used to calculate the temporal index by leveraging the $\alpha - \beta$ closure relation of the fireball external shock model (Zhang 2006; Gao et al. 2013; Wang et al. 2015). The predicted values are $\alpha = \frac{3}{2}\beta = \frac{3}{2} \times 0.8 \simeq 1.20$ for the case of constant density interstellar medium (ISM), and $\alpha = \frac{3\beta+1}{2} = \frac{3 \times 0.80 + 1}{2} \simeq 1.70$ for a wind-like case. The fitting results, $\alpha_{X,2} \approx 1.81$, and $\alpha_{R,3} \approx 1.77$, suggest a wind-like medium with the observed frequency falling within the spectral regime of $\nu_m < \nu < \nu_c$.

In addition, the long-lived optical plateau perhaps as a result of energy injection also can be tested using the closure relation. Assuming a long-lasting central engine $L(t) = L_0 (t/t_b)^{-q}$, then

¹¹ https://www.swift.ac.uk/xrt_spectra/01054681/

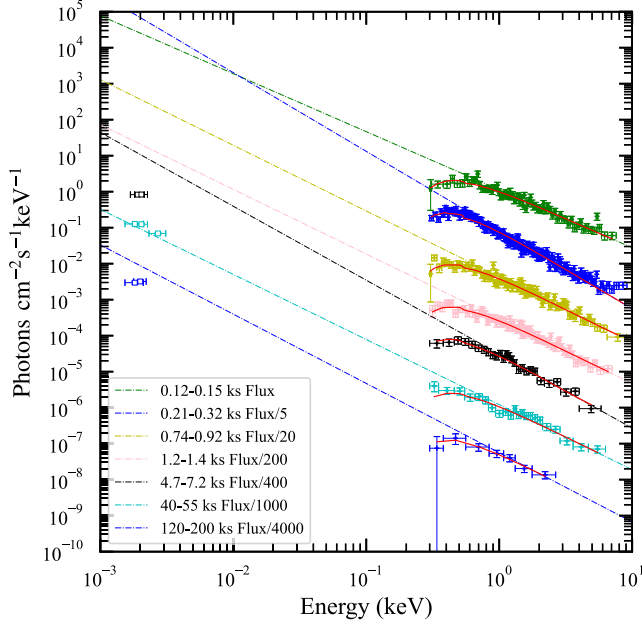


Figure 5. The results of SED analysis. The unabsorbed power-law spectrum was derived from X-ray afterglow and then extrapolated to the optical band in dotted dashed line.

Table 4
Spectral Analysis of Afterglow Emission

Slice	Interval (s)	χ_r^2	Γ_γ
1	119–147	0.91	1.61 ± 0.04
2	208–317	1.44	2.19 ± 0.02
3	743–916	0.99	1.82 ± 0.04
4	1222–1443	0.81	1.80 ± 0.04
5	4666–7164	0.66	2.05 ± 0.07
6	40022–55022	1.17	1.81 ± 0.08
7	120022–200022	0.24	1.92 ± 0.23

the dynamical evolution of fireball will be dominated by the injected energy E_{inj} when $E_{\text{inj}} > E_{\text{K,iso}}$. This scenario predicts a shallow decay with $\alpha = \frac{q}{2} + \frac{(2+q)\beta}{2}$. If the injected energy originates from the millisecond magnetar, $q=0$ is required before the characteristic timescale T and $q=-2$ after T will back to self-similar behavior according to the spin-down law (Dai & Lu 1998; Zhang & Mészáros 2001; Zhang 2006), which leads to the shallow decay slope to be 0.8. It is also in excellent agreement with our fitting result $\alpha_{\text{R},2} \sim 0.88$ in the wind-like medium, suggesting that the magnetar may indeed serve as the central engine.

A general density profile with the stratification parameter s ($s=0$ and $s=2$ reduces as ISM and wind case respectively) can be written as $n(r) = Ar^{-s}$, where $A = \frac{\dot{M}_w}{4\pi m_p v_w} \times 10^{35} A_* \text{cm}^{-1}$, in which \dot{M}_w is the mass-loss rate and v_w is the wind velocity

(Chevalier & Li 2000; Panaitescu & Kumar 2000). We proceed with a detailed analysis assuming a wind circum-burst medium.

Lin et al. (2018) suggested that central engines of GRBs might exhibit intermittent behavior, giving rise to multiple episodes of ejecta separated by a long quiescent interval. If this was the case for GRB 210610B, we consider the magnetar to be the central engine, initiating the ejection of the first ejecta, of which the internal dissipation powered the intense prompt emission, then generated the external shock as propagating into the surrounding medium. Similarly, the later-launched ejecta undergoes internal dissipation, powered the early time X-ray plateau, whose temporal profile followed the spin-down profile of the magnetar as shown above. After that, it kept propagating and eventually caught up with the blast wave decelerated by the ambient medium, thereby refreshing the blast wave. Here the energy injection term $dE_{\text{inj}}/dt_{\text{obs}}$ keeps the same form as spin-down luminosity but needs to be modified as

$$\frac{dE_{\text{inj}}}{dt_{\text{obs}}} = L_{\text{inj},0} \left(1 + \frac{t_{\text{obs}} - t_s}{T\delta} \right)^{4/1-n}, \quad (6)$$

$$t_s < t_{\text{obs}} < t_e,$$

where $L_{\text{inj},0}$ is the initial inject luminosity, t_s and t_e are the beginning and ending time of energy injection respectively. δ controls the intensity of injection.

4. Modeling: The Later-launched Ejecta Catching up with the External Shock

It has been widely recognized that the external forward shock model as a robust framework for explaining the behaviors of afterglow, especially for the cases involving with more advanced modeling (Wang et al. 2015). In our case, we adopt standard external shock proposed by Sari et al. (1998). The general dynamical evolution of the external shock is calculated following Huang et al. (1999). These equations are so concise that one can easily describe them with four coupled first-order differential equations:

$$\frac{dR}{dt_{\text{obs}}} = \frac{c\beta_j}{1 - \beta_j}, \quad (7)$$

$$\frac{dm}{dt_{\text{obs}}} = 4\pi n m_p R^2 \frac{dR}{dt_{\text{obs}}}, \quad (8)$$

$$\frac{dU'}{dt_{\text{obs}}} = (1 - \epsilon)(\Gamma - 1)c^2 \frac{dm}{dt_{\text{obs}}}, \quad (9)$$

$$\frac{d\Gamma}{dt_{\text{obs}}} = \frac{1}{M_{\text{ej}} + \epsilon m + 2(1 - \epsilon)\Gamma m} \times \left(\frac{1}{c^2} \frac{dE_{\text{inj}}}{dt_{\text{obs}}} - (\Gamma^2 - 1) \frac{dm}{dt_{\text{obs}}} \right), \quad (10)$$

where $\beta_j = \sqrt{1 - 1/\Gamma^2}$ is the velocity of the bulk fireball, m is the rest mass of the swept-up medium, U' is internal energy, ϵ is efficiency of the external shock ($\epsilon = 1$ for radiative expansion

and $\epsilon = 0$ for adiabatic expansion), and M_{ej} is the initial mass of the external shock. Sideways expansion of relativistic jet was ignored because of the unimportance of influence for flux until Γ drops below ~ 2 (Kumar & Granot 2003; van Eerten & MacFadyen 2012).

So far, there are free parameters including the isotropic kinetic energy of the burst $E_{K,iso}$, the microphysical parameters ϵ_e and ϵ_B , the initial Lorentz factor Γ_0 , A_* , $L_{inj,0}$, the starting and ending time of energy injection t_s and t_e , and the free parameter δ . The power-law index of electron distribution p was fixed as $p = 2\beta + 1 = 2.60$. There is no obvious jet-break feature, the jet opening angle $\theta_j > 5^\circ$ is given roughly due to lack jet break feature.

An MCMC method was used to fit the model to data by searching a large portion of parameter space and finding the best-fit parameters set. To facilitate this process, the emcee module was employed to handle efficiently MCMC simulations with 90 walkers for 10,000 steps (Foreman-Mackey et al. 2013). The preliminary parameters are set in the following ranges: $\log_{10} \epsilon_B \in [-5.00, -2.00]$, $\log_{10} \epsilon_e \in [-3.50, -0.60]$, $\log_{10}(E_{K,iso}/\text{erg}) \in [53.00, 54.00]$, $\log_{10} \Gamma_0 \in [2.00, 3.00]$, $\log_{10} A_* \in [-3.00, 3.00]$, $\log_{10}(L_{inj,0}/\text{erg s}^{-1}) \in [50.0, 51.0]$, $\log_{10}(t_s/s) \in [3.20, 3.90]$, $\log_{10}(t_e/s) \in [4.00, 5.50]$, $\log_{10} \delta \in [1.0, 2.0]$. The results of the MCMC method provide a set of best-fitting parameters: $\log_{10} \epsilon_B = -4.33^{+0.16}_{-0.11}$, $\log_{10} \epsilon_e = -0.81^{+0.04}_{-0.06}$, $\log_{10}(E_{K,iso}/\text{erg}) = 53.64^{+0.05}_{-0.04}$, $\log_{10} \Gamma_0 = 2.92^{+0.06}_{-0.12}$, $\log_{10} A_* = -0.99^{+0.08}_{-0.11}$, $\log_{10}(L_{inj,0}/\text{erg s}^{-1}) = 50.55^{+0.08}_{-0.07}$, $\log_{10}(t_s/s) = 3.67^{+0.01}_{-0.01}$, $\log_{10}(t_e/s) = 4.68^{+0.02}_{-0.02}$, and $\log_{10} \delta = 1.44^{+0.07}_{-0.06}$. Figure 1 shows our fitting light curve, and Figure 6 plots the results of sampling in parameters.

All the fitting parameters sit in reasonable ranges according to a large sample of GRBs (Wang et al. 2015). It is noted that $A_* \sim 0.10$ is smaller than the standard value 1, indicating a sparse surrounding density. The sparse medium means that it does not decelerate blast wave effectively, resulting in the absence of a jet break before about 11.6 days. The time when jet break appears in the stellar wind surrounding has been found by

$$t_j = 10 \times (1 + z) \left(\frac{\theta_0}{0.2} \right)^4 E_{53} A_*^{-1} \text{days}, \quad (11)$$

where E_{53} includes both the isotropic equivalent γ -ray energy and the isotropic kinetic energy of blast wave in units of 10^{53} erg, θ_0 is the opening angle of jet in units of rad. It turns out we could pose a constraint on the opening angle of jet, that is $\theta_j \geq 3.2^\circ$. Our lower limit value on opening angle is smaller than the value ($\sim 5^\circ$) inferred before (Frail et al. 2001; Bloom et al. 2003), but is consistent with the recent study (Wang et al. 2018).

Yi et al. (2022) collected 174 GRBs with X-ray plateau and 106 GRBs with X-ray flare, and analyzed the ratio of energies of X-ray plateau and flare to the isotropic prompt energy, their

results yield a Gaussian distribution with median of the logarithmic ratios to be ~ -0.96 and -1.39 in the two cases. They argue that the X-ray plateaus and flares share the common physical origin, yet manifest with distinct features resulting from varying circumstances and radiation mechanisms. Meanwhile, some studies indicate that mass-loaded jets (“dirty fireball”; Paczyński 1998; Dermer et al. 1999) with the initial Lorentz factor below $\Gamma_{init} \sim 100$ could have lower peak at energy, thus appear as the prompt X-ray emission instead (Dermer et al. 1999; Heise et al. 2001; Zhang et al. 2004; Sakamoto et al. 2005; Soderberg et al. 2007; Ho et al. 2022). Make an aggressive assumption that it could be a similar scenario for the early X-ray plateau. As such, the Lorentz factor of the later launched ejecta would not be too large in GRB 210610B. Based on an interesting implication of t_s , the time of the later launched ejecta lags behind the photon formed at the internal dissipation radius (R_{dis}) and at the injected radius (R_{inj}), we deduce that the average Lorentz factor of the later launched ejecta is related to $R_{inj}/2\Gamma_2^2 c \sim t_s/(1+z)$, which gives $\Gamma_2 \sim 51$. It should be noted that the Lorentz factor Γ_2 is a lower limit because of the implied treatment of launching incessantly ejects. In other words, the later launched ejecta needs a larger Lorentz factor to catch up with the blast burst at R_{inj} .

The GRB radiative efficiency $\eta_\gamma = E_{\gamma,iso}/(E_{\gamma,iso} + E_{K,iso}) = 56.0\%$ reflect the efficiency of the internal dissipation within the first ejecta. For the later ejecta, the efficiency of the internal dissipation can be estimated as $\eta_X \sim L_X T / (L_X T + E_{inj})$, where the injected isotropic energy can be obtained by integrating dE_{inj}/dt_{obs} from t_s to t_e :

$$\frac{1}{1+z} \int_{t_s}^{t_e} \frac{dE_{inj}}{dt_{obs}} dt_{obs} \quad (12)$$

which yields $E_{inj} = 2.0 \times 10^{54}$ ergs and thereof $\eta_X \sim 0.1\%$.

One can obtain plateau parameters after beaming correction by:

$$L_0 = \frac{L_X}{\eta_X} f_b \quad (13)$$

where $f_b = (1 - \cos \theta_j)$ is beaming correction factor. Parameters of a millisecond magnetar can be inferred after taking the standard values of $I_{45} \sim 1$ and $R_6 \sim 1$, the initial spin period $P \sim 2.6$ ms and the surface polar cap magnetic field strength $B \sim 3.2 \times 10^{15}$ G, which are among the GRBs magnetar population (Lü & Zhang 2014).

5. Conclusions and Discussion

GRB 210610B was detected by both Swift/BAT and Fermi/GBM as well as HXMT/HE, showing multi-pulse profiles. Its afterglow light curves show discrete plateaus from broadband follow-up observations. We summarize our main conclusions as follows from both temporal and spectral analyses.

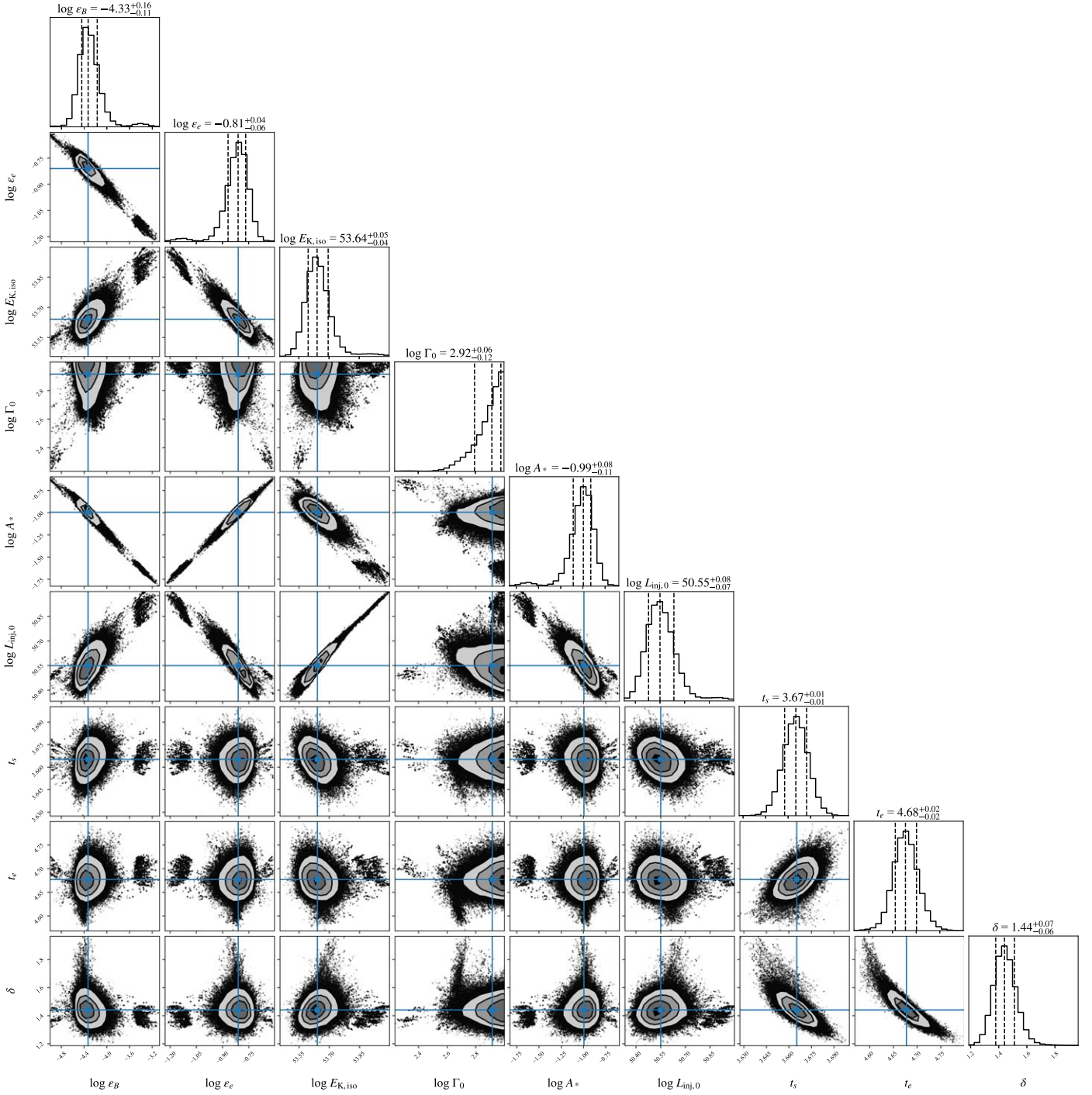


Figure 6. Corner plot showing the results of MCMC sampling.

1. We employ the Band function to fit both the time-resolved spectra and time-integrated spectrum, a set of parameters derived from the latter (with $\hat{\alpha} = -0.47 \pm 0.05$, $\hat{\beta} = -2.73 \pm 0.22$ and $E_p = 305 \pm 24$ keV) can be used to calculate the isotropic γ -ray energy $E_{\gamma,iso} = (5.55 \pm$

$0.78) \times 10^{53}$ ergs in the 1–10000 keV band (rest frame), which falls into the long GRB Amati relation.

2. The SEDs between X-ray and optical afterglow have no obvious evolution with an averaged value of the photon index $\Gamma_\gamma \approx 1.80$. The early X-ray lightcurve exhibits a

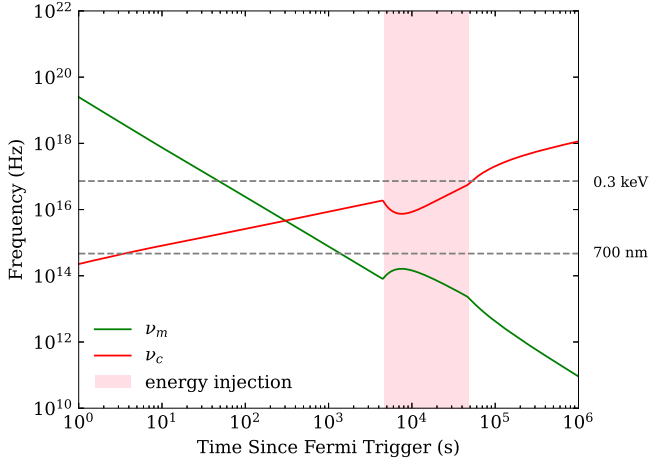


Figure 7. Synchrotron parameters ν_m and ν_c vary with time. Energy injection in the pink shaded region refreshes the blast wave making synchrotron parameters change.

plateau followed by a steep decay that can be reasonably fitted with $F_X = (1+z)(\eta_X L_{EM} + At^{-\alpha})/(4\pi D_L^2)$, which gives $n \approx 3.04$.

3. The temporal and spectral joint fits of the multiwavelength light curves of GRB 210610B indicate that the external shock spread in the staller-wind medium, and the energy injection model can describe the behavior of afterglow. The best parameters are $\log_{10} \epsilon_B \approx -4.33$, $\log_{10} \epsilon_e \approx -0.81$, $\log_{10} E_{K,iso} \approx 53.64$ erg, $\log_{10} \Gamma_0 \approx 2.92$, $\log_{10} A_* \approx -0.99$ cm⁻³, $\log_{10} L_{inj,0} \approx 50.55$ erg s⁻¹, $\log_{10} t_l \approx 3.67$ s, $\log_{10} t_e \approx 4.68$ s, $\log_{10} \delta \approx 1.44$.

Noting that we did not make the deep-going spectral analysis of GRB 210610B. Chen et al. (2022) presented results of the spectral, that 76% of the spectra need an additional thermal component to obtain a better fit. It indicates that the Poynting flux component may play an important role in addition to the hot fireball component. Our results deduce from the aspect the afterglow phase, which suggested that the magnetar serves as the central engine of GRB 210610B. Both results of this work and Chen et al. (2022) are consistent with each other.

We have tried to incorporate the early *R* band data (before 6ks) for our model and found that it fits well, which suggests the early optical data is primarily contributed by the external forward shock with the observed frequency $\nu_a < \nu_R < \nu_m$. To conceptualize, we have traced the synchrotron parameters and illustrated them in Figure 7. One can see the light curve change smoothly owing to the curvature effect as observing frequency ν_R across the characteristic frequency ν_m . For the early evolution of blast wave, the fast cooling and synchrotron self-absorption may play significant roles, a quick follow-up optical observation with multiwavelength can be used to certify the complicated situation.

Acknowledgments

We thank the anonymous referee of this work for useful comments and suggestions that improved the paper. This work was funded by the National Natural Science Foundation of China (Nos. 12373042, U1938201, 12273005 and 12133003), the Programme of Bagui Scholars Programme (WXG). We also thank the support of the China Space Station Telescope (CSST). The authors are very grateful to the public GRB Fermi/GBM, Swift and HXMT data.

ORCID iDs

- Xiang-Gao Wang (王祥高) <https://orcid.org/0000-0001-8411-8011>
 Da-Bin Lin (林达斌) <https://orcid.org/0000-0003-1474-293X>
 Wei-Kang Zheng (郑伟康) <https://orcid.org/0000-0002-2636-6508>
 Liang-Jun Chen (陈良军) <https://orcid.org/0009-0007-7188-3196>
 Shuang-Xi Yi (仪双喜) <https://orcid.org/0000-0003-0672-5646>
 En-Wei Liang (梁恩维) <https://orcid.org/0000-0002-7044-733X>

References

- Abbott, B. P., Abbott, R., Abbott, T. D., et al. 2017, *ApJL*, **848**, L13
 Amati, L., Frontera, F., Tavani, M., et al. 2002, *A&A*, **390**, 81
 Band, D., Matteson, J., Ford, L., et al. 1993, *ApJ*, **413**, 281
 Berger, E. 2014, *ARA&A*, **52**, 43
 Bloom, J. S., Frail, D. A., & Kulkarni, S. R. 2003, *ApJ*, **594**, 674
 Chen, J.-M., Peng, Z.-Y., Du, T.-T., & Yin, Y. 2022, *ApJ*, **932**, 25
 Chevalier, R. A., & Li, Z.-Y. 2000, *ApJ*, **536**, 195
 Costa, E., Frontera, F., Heise, J., et al. 1997, *Nature*, **387**, 783
 Dai, Z. G., & Lu, T. 1998, *A&A*, **333**, L87, T.
 de Ugarte Postigo, A., Thoene, C., Agui Fernandez, J. F., et al. 2021, GCN, **30194**, 1
 Dermer, C. D. 2004, *ApJ*, **614**, 284
 Dermer, C. D., Chiang, J., & Böttcher, M. 1999, *ApJ*, **513**, 656
 Eichler, D., Livio, M., Piran, T., & Schramm, D. N. 1989, *Natur*, **340**, 126
 Evans, P. A., Willingale, R., Osborne, J. P., et al. 2010, *A&A*, **519**, A102
 Fenimore, E. E., Madras, C. D., & Nayakshin, S. 1996, *ApJ*, **473**, 998
 Foreman-Mackey, D., Hogg, D. W., Lang, D., & Goodman, J. 2013, *PASP*, **125**, 306
 Frail, D. A., Kulkarni, S. R., Nicastro, L., Feroci, M., & Taylor, G. B. 1997, *Natur*, **389**, 261
 Frail, D. A., Kulkarni, S. R., Sari, R., et al. 2001, *ApJ*, **562**, L55
 Gao, H., Lei, W.-H., Zou, Y.-C., Wu, X.-F., & Zhang, B. 2013, *NewAR*, **57**, 141
 Gehrels, N., Sarazin, C. L., O'Brien, P. T., et al. 2005, *Natur*, **437**, 851
 Heise, J., Zand, J. I., Kippen, R. M., & Woods, P. M. 2001, in *Gamma-ray Bursts in the Afterglow Era*, ed. E. Costa, F. Frontera, & J. Hjorth (Berlin: Springer), 16
 Ho, A. Y. Q., Perley, D. A., Yao, Y., et al. 2022, *ApJ*, **938**, 85
 Huang, Y. F., Dai, Z. G., & Lu, T. 1999, *MNRAS*, **309**, 513
 Ibrahimov, M., Nalivkin, M., Nikolenko, I., Pons, O. & a larger Team 2021, GCN, **30226**, 1
 Krimm, H. A., Barthelmy, S. D., Cummings, J. R., et al. 2021, GCN, **30207**, 1
 Kumar, P., & Granot, J. 2003, *ApJ*, **591**, 1075
 Kumar, P., & Panaitescu, A. 2000, *ApJL*, **541**, L51

- Liang, E.-W., Lü, H.-J., Hou, S.-J., Zhang, B.-B., & Zhang, B. 2009, *ApJ*, **707**, 328
- Liang, E.-W., Racusin, J. L., Zhang, B., Zhang, B.-B., & Burrows, D. N. 2008, *ApJ*, **675**, 528
- Liang, E. W., Zhang, B., O'Brien, P. T., et al. 2006, *ApJ*, **646**, 351
- Liang, E.-W., Zhang, B.-B., & Zhang, B. 2007, *ApJ*, **670**, 565
- Lin, D.-B., Huang, B.-Q., Liu, T., et al. 2018, *ApJ*, **852**, 136
- Lü, H.-J., & Zhang, B. 2014, *ApJ*, **785**, 74
- Lyons, N., O'Brien, P. T., Zhang, B., et al. 2010, *MNRAS*, **402**, 705
- Malacaria, C., Hristov, B. & Fermi GBM Team 2021, GCN, 30199, 1
- Marchini, A., Lorini, A., Leonini, S., & Bonoli, G. 2021, GCN, 30198, 1
- Moskvitin, A. S. & GRB follow-up Team 2021, GCN, 30187, 1
- Moskvitin, A. S., Maslennikova, O. A. & GRB follow-up Team 2021, GCN, 30230, 1
- Nissinen, M., & Oksanen, A. 2021, GCN, 30231, 1
- Noto, R., Hosokawa, R., Murata, K. L., et al. 2021, GCN, 30220, 1
- Nousek, J. A., Kouveliotou, C., Grupe, D., et al. 2006, *ApJ*, **642**, 389
- Paczynski, B. 1991, *AcA*, **41**, 257
- Paczyński, B. 1998, *ApJL*, **494**, L45
- Page, K. L., Gropp, J. D., Kennea, J. A., et al. 2021, GCN, 30170, 1
- Panaiteescu, A., & Kumar, P. 2000, *ApJ*, **543**, 66
- Pankov, N., Nazarov, S., Pozanenko, A., Belkin, S. & IKI GRB FuN 2021a, GCN, 30988, 1
- Pankov, N., Pozanenko, A., Inasaridze, R. Y., et al. 2021b, GCN, 30243, 1
- Pankov, N., Pozanenko, A., Rummyantsev, V., Belkin, S., & GRB FuN, I. 2021c, GCN, 30245, 1
- Pankov, N., Pozanenko, A., Rummyantsev, V., Belkin, S., & GRB FuN, I. 2021d, GCN, 30213, 1
- Pei, Y. C. 1992, *ApJ*, **395**, 130
- Pozanenko, A., & Elenin, L. 2013, *EAS Pub. Ser.*, **61**, 319
- Qin, Y.-P., Zhang, Z.-B., Zhang, F.-W., & Cui, X.-H. 2004, *ApJ*, **617**, 439
- Racusin, J. L., Liang, E. W., Burrows, D. N., et al. 2009, *ApJ*, **698**, 43
- Romanov, F. D. 2021, GCN, 30181, 1
- Romanov, F. D., & Lane, D. J. 2021, GCN, 30228, 1
- Rummyantsev, V., Pozanenko, A., Belkin, S., Pankov, N. & GRB IKI FuN 2021, GCN, 30178, 1
- Sakamoto, T., Lamb, D. Q., Kawai, N., et al. 2005, *ApJ*, **629**, 311
- Sari, R., Piran, T., & Narayan, R. 1998, *ApJL*, **497**, L17
- Schlafly, E. F., & Finkbeiner, D. P. 2011, *ApJ*, **737**, 103
- Soderberg, A. M., Nakar, E., Cenko, S. B., et al. 2007, *ApJ*, **661**, 982
- Troja, E., Cusumano, G., O'Brien, P. T., et al. 2007, *ApJ*, **665**, 599
- van Eerten, H. J., & MacFadyen, A. I. 2012, *ApJL*, **747**, L30
- van Paradijs, J., Groot, P. J., Galama, T., et al. 1997, *Natur*, **386**, 686
- Vreeswijk, P. M., & Broens, E. 2021, GCN, 30205, 1
- Wang, X.-G., Zhang, B., Liang, E.-W., et al. 2015, *ApJS*, **219**, 9
- Wang, X.-G., Zhang, B., Liang, E.-W., et al. 2018, *ApJ*, **859**, 160
- Willingale, R., O'Brien, P. T., Osborne, J. P., et al. 2007, *ApJ*, **662**, 1093
- Woosley, S. E. 1993, *ApJ*, **405**, 273
- Woosley, S. E., & Bloom, J. S. 2006, *ARA&A*, **44**, 507
- Yang, J., Ai, S., Zhang, B.-B., et al. 2022, *Natur*, **612**, 232
- Yi, S.-X., Du, M., & Liu, T. 2022, *ApJ*, **924**, 69
- Yu, Y. B., Wu, X. F., Huang, Y. F., et al. 2015, *MNRAS*, **446**, 3642
- Zhang, B. 2006, *Natur*, **444**, 1010
- Zhang, B. 2018, *The Physics of Gamma-Ray Bursts* (Cambridge: Cambridge Univ. Press)
- Zhang, B., Fan, Y. Z., Dyks, J., et al. 2006, *ApJ*, **642**, 354
- Zhang, B., Liang, E., Page, K. L., et al. 2007b, *ApJ*, **655**, 989
- Zhang, B., & Mészáros, P. 2001, *ApJL*, **552**, L35
- Zhang, B., Zhang, B.-B., Liang, E.-W., et al. 2007a, *ApJL*, **655**, L25
- Zhang, B., Zhang, B.-B., Virgili, F. J., et al. 2009, *ApJ*, **703**, 1696
- Zhang, W., Woosley, S. E., & Heger, A. 2004, *ApJ*, **608**, 365
- Zheng, W., Filippenko, A. V. & KAIT GRB Team 2021a, GCN, 30227, 1
- Zheng, W., Filippenko, A. V. & KAIT GRB Team 2021b, GCN, 30204, 1